

Article

Spark Plasma Sintering of Tungsten Oxides WO_x ($2.50 \leq x \leq 3$): Phase Analysis and Thermoelectric Properties

Felix Kaiser ^{1,*}, Paul Simon ¹, Ulrich Burkhardt ¹, Bernd Kieback ², Yuri Grin ¹ and Igor Veremchuk ^{1,*} 

¹ Max-Planck-Institut für Chemische Physik fester Stoffe, 01187 Dresden, Germany; paul.simon@cpfs.mpg.de (P.S.); burkhardt@cpfs.mpg.de (U.B.); grin@cpfs.mpg.de (Y.G.)

² Fraunhofer Institut für Fertigungstechnik und Angewandte Materialforschung, 01277 Dresden, Germany; bernd.kieback@ifam-dd.fraunhofer.de

* Correspondence: felix.kaiser@cpfs.mpg.de (F.K.); igor.veremchuk@cpfs.mpg.de (I.V.); Tel.: +49-351-4646-4000 (F.K. & I.V.)

Academic Editor: George S. Nolas

Received: 26 July 2017; Accepted: 23 August 2017; Published: 5 September 2017

Abstract: The solid-state reaction of WO_3 with W was studied in order to clarify the phase formation in the binary system W-O around the composition WO_x ($2.50 \leq x \leq 3$) during spark plasma sintering (SPS). A new phase “ $WO_{2.82}$ ” is observed in the range $2.72 \leq x \leq 2.90$ which might have the composition $W_{12}O_{34}$. The influence of the composition on the thermoelectric properties was investigated for $2.72 \leq x \leq 3$. The Seebeck coefficient, electrical conductivity and electronic thermal conductivity are continuously tunable with the oxygen-to-tungsten ratio. The phase formation mainly affects the lattice thermal conductivity κ_{lat} which is significantly reduced until 700 K for the sample with the composition $x = 2.84$, which contains the phases $W_{18}O_{49}$ and “ $WO_{2.82}$ ”. In single-phase $WO_{2.90}$ and multi-phase WO_x materials ($2.90 \leq x \leq 3$), which contain crystallographic shear plane phases, a similar reduced κ_{lat} is observed only below 560 K and 550 K, respectively. Therefore, the composition range $x < 2.90$ in which the pentagonal column structural motif is formed might be more suitable for decreasing the lattice thermal conductivity at high temperatures.

Keywords: thermoelectric materials; spark plasma sintering; tungsten oxides; crystallographic shear plane phases

1. Introduction

Transition metal oxides (TMOs) are under debate for high-temperature thermoelectric (TE) applications since $NaCo_2O_4$ was found to be a *p*-type material with a thermopower α as high as $100 \mu V \cdot K^{-1}$ at 300 K [1]. By now, TMOs are subject of in-depth investigations [2–4] in particular because there is still a lack of appropriate *n*-type counterparts, although lanthanum-doped $SrTiO_3$ [5], ZnO [6] or doped TiO_{2-x} [7–9] show promising results.

The enhancement of a TE material’s figure-of-merit ZT (Equation (6)) might be obtained by either increasing the power factor $\alpha^2\sigma$ or decreasing the total thermal conductivity $\kappa_{tot} = \kappa_{el} + \kappa_{lat}$ (Equations (3) and (4)). An interesting approach is the exploitation of crystallographic shear (CS) for the reduction of the lattice thermal conductivity κ_{lat} due to increased phonon scattering [4,10,11]. CS plane structures occur when a transition metal is partially reduced and oxygen layers are removed from the structure, e.g., of TiO_2 , VO_2 , MoO_3 and WO_3 . In the tungsten-oxygen system (Figure 1a) with decreasing O/W-ratio x the observed phases are the insulating ReO_3 -type WO_3 , the semiconducting phase $W_{20}O_{58}$ with CS planes, the metallic phase $W_{18}O_{49}$ with pentagonal columns (PC) and the

metallic rutile-type WO_2 , with varying coupling of the $[\text{WO}_6]$ octahedra (Figure 1b–e). Such structure modifications result in an increasing charge carrier concentration [12]. A further five observed phases in the range $2 < x < 3$ are predicted to be bad metals with charge carrier densities of the order 10^{21} – 10^{22} cm^{-1} according to band structure calculations [13]. Yet, these phases occur only in small domains of single crystals [14,15] or under high pressure conditions [16–18]. The fact that they are not observed as bulk materials might be attributed to a microstrain-driven ordering mechanism of the CS planes [19], which should be sensitive to the synthesis conditions.

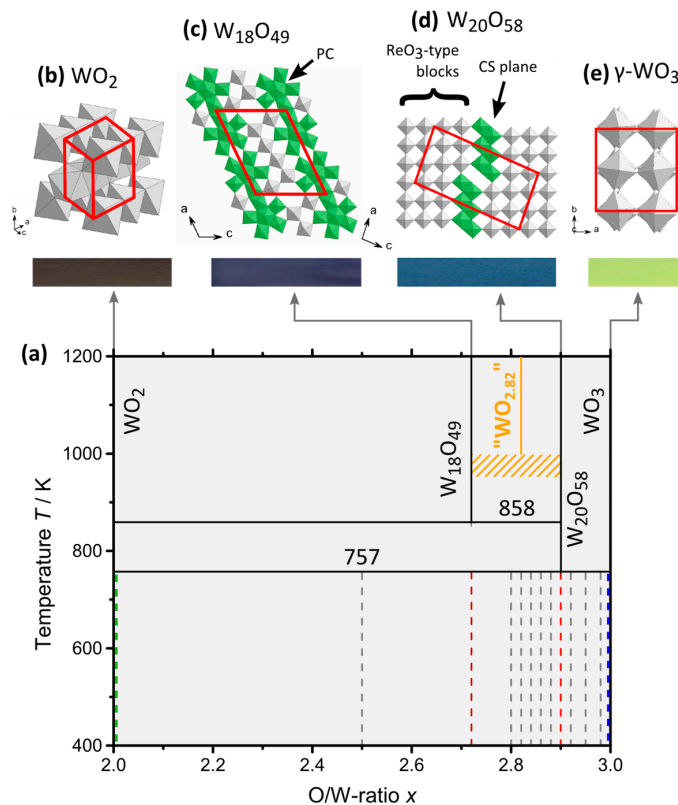


Figure 1. (a) Phase diagram of the binary system W-O in the range of the O/W-ratio $2 \leq x \leq 3$ [20]. Dashed lines mark the sample compositions prepared and characterized in this work. A metastable phase “ $\text{WO}_{2.82}$ ” (orange) is found; (b–e) Crystal structures and respective colors of the known tungsten oxide phases. Characteristic features are the $[\text{WO}_6]$ octahedra (grey), pentagonal columns (PC) and crystallographic shear (CS) planes (green). For clarity, only the monoclinic $\gamma\text{-WO}_3$ is shown among the WO_3 modifications.

The vapor-transport preparation route to obtain these phases comprises a high-temperature heating of WO_x powder mixtures over several days and weeks [14,15,21–23]. Recently $\text{WO}_{2.72}$ ($\text{W}_{18}\text{O}_{49}$) and $\text{WO}_{2.90}$ ($\text{W}_{20}\text{O}_{58}$) were successfully prepared by spark plasma sintering (SPS) being promising bulk TE materials [11,12,24]. SPS combines the solid-state reaction of powdered precursor mixtures with simultaneous shaping, and provides an effective manufacturing route for TE materials due to low temperatures and short reaction times [8]. The samples around the composition $\text{WO}_{2.90}$ still showed the formation of a further phase which was interpreted as $\text{WO}_{2.96}$ [25].

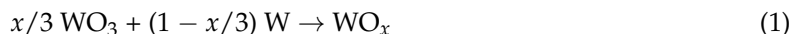
The knowledge on phase formation in the tungsten-oxide system under SPS conditions still appears fragmentary which complicates the evaluation of the system’s potential as a TE material. Thus, we studied the products of the SPS redox reaction dependent on both, the composition x in the range $2.50 \leq x \leq 3$ (Figure 1a, dashed lines) and the synthesis temperature T_{max} with powder X-ray diffraction (PXRD). Subsequently, the TE properties of the SPS-prepared WO_x materials with $x \geq 2.72$ were investigated.

In this work we use the notation “ WO_x ” for sample compositions, and “ W_aO_b ” for phases and their crystal structures.

2. Results & Discussion

2.1. Spark Plasma Preparation

The solid-state reaction



was performed for different x by spark plasma sintering (SPS) in vacuum (<10 Pa) under an uniaxial pressure of 80 MPa (Figure 2a). Temperature programs included a linear heating with $50 \text{ K}\cdot\text{min}^{-1}$, an isothermal dwell time t_{dwell} at the temperature T_{max} , and free cooling. Specific experiments in this work are notated by “SPS- $T_{\text{max}}/t_{\text{dwell}}$ ”.

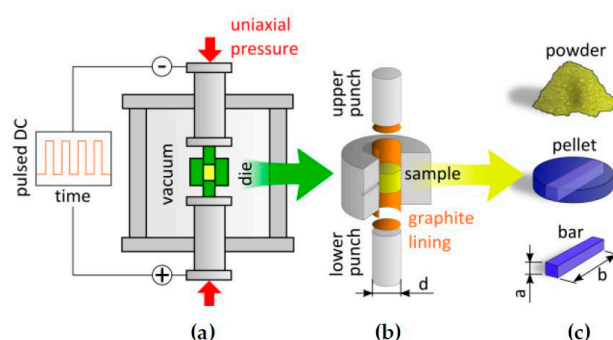


Figure 2. (a) Setup of the spark plasma sintering (SPS) machine; (b) Scheme of the filled SPS die; (c) Sample powder reacted in the SPS and compacted to pellets. For measurements tetragonal bars with a ≈ 1.5 mm and $b \approx 6$ –8 mm were cut.

For the reference material $\text{WO}_{2.90}$, the SPS treatment was optimized regarding the phase purity. Systematic variations of the temperature and dwell time in the ranges $1320 \text{ K} \leq T_{\text{max}} \leq 1570 \text{ K}$ and $10 \text{ min} \leq t_{\text{dwell}} \leq 4 \text{ h}$, respectively, yielded the optimum regime SPS-1420 K/10 min (Figure 3b). Samples WO_x with $x = \{2.50, 2.72, 2.80, 2.82, 2.84, 2.86, 2.88, 2.92, 2.95, 2.98\}$ were prepared with the same conditions.

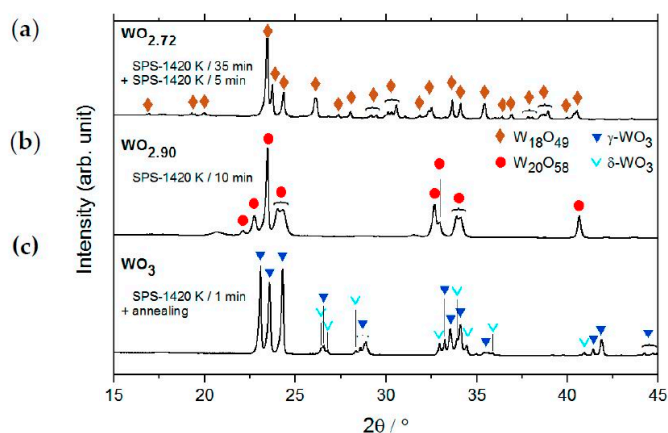


Figure 3. PXRD patterns (Cu- $\text{K}\alpha_1$ radiation) of the reference materials obtained by SPS: (a) Single-phase $\text{WO}_{2.72}$ after two-step treatment with surface cleaning and grinding in between; (b) Single-phase $\text{WO}_{2.90}$ after one-step treatment; (c) WO_3 sample contains two modification γ - and δ - WO_3 after SPS and subsequent annealing in open air (1170 K, 68 h).

Phase-pure reference material $WO_{2.72}$ was obtained via SPS-1420 K/35 min followed by SPS-1420 K/5 min with cleaning of the surface and grinding of the sample between both steps (Figure 2a).

A WO_2 reference sample was directly compacted from the as-purchased material with SPS-1470 K/10 min (green curve in Figure 4).

The compaction of the yellowish as-purchased material WO_3 with SPS-1420 K/10 min resulted in a bluish-violet and multiple-phase product according to PXRD (blue curve in Figure 4). Subsequent annealing performed at 1170 K for 68 h in the open air was supposed to yield the monoclinic γ - WO_3 [26] and resulted in a greyish-yellow specimen (Figure 3c).

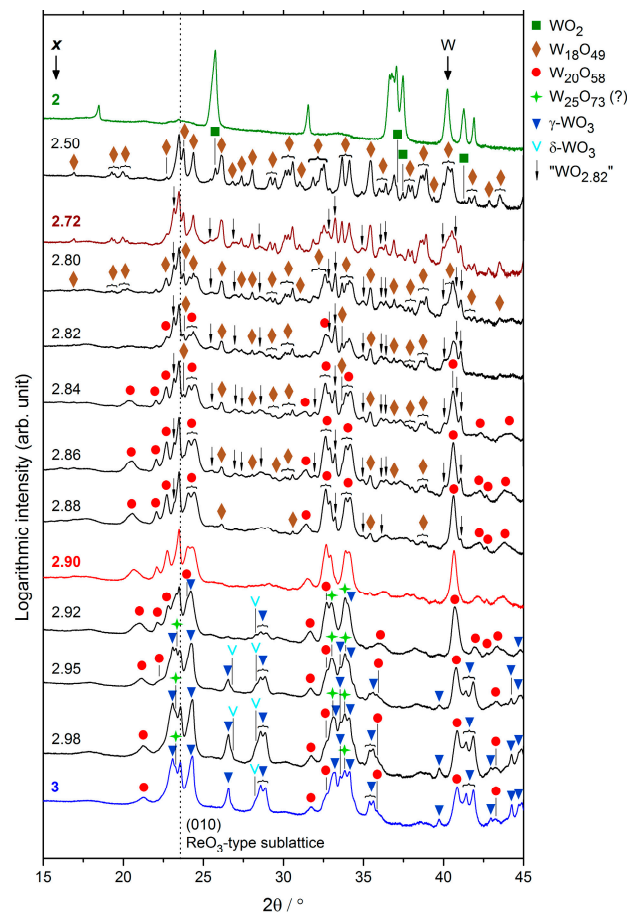


Figure 4. PXRD patterns (Cu- $K_{\alpha 1}$ radiation) of the WO_x samples processed with SPS-1420/10 min. Only the WO_2 reference sample was compacted with SPS-1470 K/10 min (green line).

2.2. Single-Phase Materials WO_2 , $WO_{2.72}$, $WO_{2.90}$ and WO_3

According to PXRD, phase-pure material $WO_{2.72}$ is obtained from the two-step treatment (Figure 3a).

Phase-pure material $WO_{2.90}$ is yielded from the routine SPS-1420 K/10 min as seen from the PXRD pattern (Figure 3b), which shows only reflections of $W_{20}O_{58}$ ($x = 2.90$). However, all reflections except $(0\ k\ 0)$ show large FWHM values indicating good ordering only in the $[010]$ direction (Figure 1d). Starting from this optimized regime for $x = 2.90$, the increase of both T_{\max} and t_{dwell} promotes the formation of $W_{18}O_{49}$ ($x = 2.72$), WO_2 and an additional phase. We ascribe the composition $x \approx 2.82$ for this phase as seen in the following. Thus, the schematic secondary reaction



represents a further tungsten reduction below $x = 2.90$ and is probably a similar SPS-specific reduction effect which is observed for pure WO_3 . However, in the case of $\text{W}_{20}\text{O}_{58}$ a further decomposition can be kinetically inhibited with a short SPS treatment time $t_{\text{dwell}} = 10$ min.

The WO_2 does not undergo changes during the SPS treatment. A minor amount of elemental tungsten is observed in both, the as-purchased and SPS-processed material (green curve in Figure 4).

The as-purchased WO_3 sample is confirmed to adopt monoclinic structure ($\gamma\text{-WO}_3$). In contrast, the PXRD pattern after SPS treatment (SPS-1420 K/10 min, blue curve in Figure 4) shows a mixture of $\gamma\text{-WO}_3$ (blue triangles), triclinic $\delta\text{-WO}_3$ (cyan arrows), $\text{W}_{20}\text{O}_{58}$ ($x = 2.90$, red dots), and an additional phase (green stars) whose reflections resemble those of $\text{W}_{25}\text{O}_{73}$ ($x = 2.92$) [14]. The $\delta\text{-WO}_3$ is the stable modification below 290 K [27]. Conventional preparation of WO_3 via high-temperature oxidation usually yields $\gamma\text{-WO}_3$ [28] whereas the conditions during the free cooling in the SPS processing could promote the further transition $\gamma \rightarrow \delta$. After annealing in open air (1170 K, 68 h), only γ - and $\delta\text{-WO}_3$ is found in the reference sample (Figure 3c). Most possibly, the annealing time was not sufficient to complete the $\delta \rightarrow \gamma$ transformation, or the cooling rate afterwards was not sufficient to suppress the $\gamma \rightarrow \delta$ transition completely. No clear evidence is found for the existence of $\text{W}_{25}\text{O}_{73}$ due to strong reflection overlapping. Yet, a reducing influence of the SPS graphite die and lining on the WO_3 starting material is clearly seen from the formation of $\text{W}_{20}\text{O}_{58}$. It is supposed to appear at ≈ 1020 K [29] and occurs despite the short $t_{\text{dwell}} = 10$ min and even 1 min. This SPS specific reduction should be considered additionally to the reaction with W, and will result in WO_x samples with compositions slightly deviating from the nominal O/W-ratio x .

The refined lattice parameters of the as-purchased materials and obtained single-phase products are given in Table 1 together with the respective literature data.

Table 1. Lattice parameters of phases in the tungsten–oxygen binary system refined from PXRD patterns in this work in comparison to literature data (iv—long-term heating in vacuo, SPS—spark plasma sintering, n.a.—not specified in the reference).

| x | Phase | Source | Space Group | Lattice Parameters | | | | | Ref. | |
|------|------------------------------|------------------|-------------|--------------------|----------|-----------|-----------|----------------|-----------|--|
| | | | | a | b | c | β | V | | |
| | | | | Å | Å | Å | deg | Å ³ | | |
| 2 | WO_2 | n.a. | $P2_1/c$ | 5.58 | 4.90 | 5.664 | 120.7 | 133.1 | [30] | |
| | | commercial SPS | | 5.574(1) | 4.898(1) | 5.662(1) | 120.69(1) | 132.9(2) | this work | |
| 2.72 | $\text{W}_{18}\text{O}_{49}$ | n.a. | $P2/m$ | 18.32 | 3.79 | 14.04 | 115.0 | 883.3 | [31] | |
| | | iv | | 18.33 | 3.79 | 14.04 | 115.2 | 882.1 | [32] | |
| | | n.a. | | 18.32 | 3.78 | 14.03 | 115.2 | 879.5 | [33] | |
| | | SPS | | 18.32 | 3.79 | 14.04 | n/a | — | [11] | |
| 2.83 | $\text{W}_{12}\text{O}_{34}$ | n.a. | $P2/m$ | 17.0 | 3.8 | 19.4 | 105.3 | — | [34] | |
| | | SPS ^a | | 17.229(1) | 3.782(1) | 19.496(1) | 105.77(1) | 1223(3) | this work | |
| 2.90 | $\text{W}_{20}\text{O}_{58}$ | iv | $P2/m$ | 12.1 | 3.78 | 23.4 | 85 | 1066.2 | [21] | |
| | | calculated | | 12.05 | 3.77 | 23.59 | 85.3 | 1067.2 | [35] | |
| | | SPS | | 12.08 | 3.78 | 23.59 | n/a | — | [11] | |
| | | SPS | | 12.00 | 3.78 | 23.51 | 84.8 | 1062.0 | [24] | |
| 2.92 | $\text{W}_{25}\text{O}_{73}$ | iv | $P2/c$ | 11.93 | 3.82 | 59.72 | 98.3 | 2693.1 | [14] | |
| | | SPS | | 12.080(3) | 3.782(1) | 23.62(1) | 85.36(1) | 1075.6(7) | this work | |
| 3 | $\gamma\text{-WO}_3$ | commercial | $P2_1/n$ | 7.33 | 7.56 | 7.73 | 90.5 | 428.3 | [36] | |
| | | commercial | | 7.299(1) | 7.537(1) | 7.689(1) | 90.88(1) | 422.9(1) | this work | |

^a Parameters determined from only 10 main reflections.

2.2.1. Crystal Structure on Atomic Resolution

From high-resolution transmission electron microscopy (HR-TEM) along [001] of the single-phase $\text{WO}_{2.90}$, large ordering areas are observed (Figure 5a). The zoomed and Fourier-filtered image from the top-left area (Figure 5b), and the corresponding fast Fourier transform (FFT) reveal the expected values of the lattice parameters a and b , but also some superstructure reflections indicating the doubling of

the lattice parameter c (Figure 5c). In [010] direction, CS planes are visible but massively disordered with varying alignments and spacing (Figure 5d) which are consistent with the large FWHM values in the PXRD pattern (Figure 4a). The zoomed and filtered image (Figure 5e) shows low ordering along [001], where only the (001) reflection is present, whereas along [100], reflections of the fifth- and even higher order are observed in the FFT image (Figure 5f).

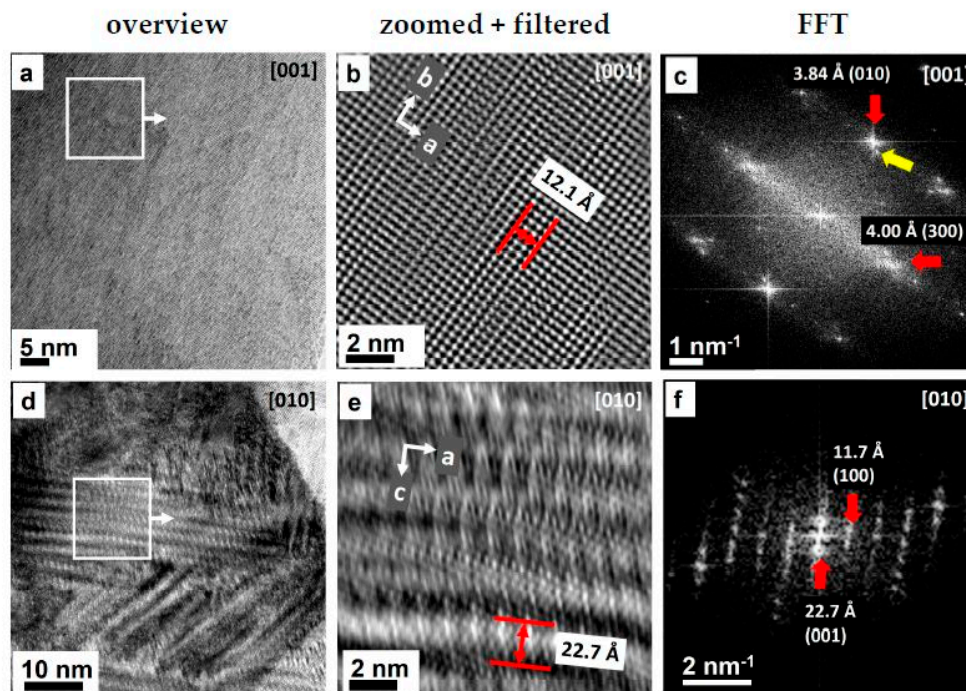


Figure 5. HR-TEM images of SPS-prepared $\text{WO}_{2.90}$ material along (a–c) [001] and (d–f) [010]. (a) Good ordering is found for the zone [001]; (b) The Fourier-filtered micrograph reveals a lattice with long-range variations; (c) Yellow-marked reflections in the corresponding FFT image indicate a superstructure; (d) CS planes are found for the [010] zone, however massive disorder is observed with deviations of CS plane orientations of about 44° ; (e) Zooming and filtering reveals short-range order along [001]; (f) FFT with broadened and diffuse (001) reflection confirms disturbance of the atomic arrangement along [001].

2.2.2. Thermoelectric Properties

Among the known phases, the lowest electrical conductivity $\sigma(T)$ values are measured for $\text{WO}_{2.90}$ with $77(3) \times 10^3 \text{ S}\cdot\text{m}^{-1}$ over the whole temperature range, which is on the level of a heavily doped semiconductor (Figure S1a). A local maximum at 635 K is in good accordance with previous records [11,12,24]. The electrical conductivity of WO_2 and $\text{WO}_{2.72}$ indicates typical metallic behaviour with $\sigma(T) \propto 1/T$ dependency (Figure S1b). No electrical transport measurement was possible for the compacted and annealed WO_3 sample due to its insulating behaviour. This indicates the absence of oxygen vacancies after SPS and annealing, which would promote the electrical conductivity [37].

Both metallic samples (WO_2 and $\text{WO}_{2.72}$) reveal a relative high thermal conductivity $\kappa_{\text{tot}}(T) > 10 \text{ W}\cdot\text{m}^{-1}\cdot\text{K}^{-1}$ (Figure 6a). However, in the dense WO_2 structure (Figure 1b), where strong tungsten–tungsten interactions are expected, this arises mainly from the lattice contribution κ_{lat} , whereas in $\text{WO}_{2.72}$ κ_{el} and κ_{lat} contribute equally (Figure 6b). For the electrically insulating WO_3 sample ($\kappa_{\text{lat}} = \kappa_{\text{tot}}$), the temperature dependence $\kappa_{\text{lat}}(T)$ appears similar to that of $\text{WO}_{2.72}$. However, for $\text{WO}_{2.72}$ the approximation of κ_{lat} shows uncertainty of maximum 45% and a significant difference regarding WO_3 cannot be determined.

WO_{2.90} shows $\kappa_{\text{tot}} \approx 3.5\text{--}4.5 \text{ W}\cdot\text{m}^{-1}\cdot\text{K}^{-1}$ over the whole temperature range (Figure 6a), which is close to previously published values [11,24]. With respect to errors its lattice contribution κ_{lat} equals that of WO₃ for $T > 560 \text{ K}$ (Figure 6b). Thus, the effect of CS planes in the W₂₀O₅₈ structure on the lattice thermal conductivity appears insignificant at high temperatures. The pentagonal column (PC) structural motif of the W₁₈O₄₉ phase (Figure 1c) in WO_{2.72} might be an alternative phonon scattering center but proof requires a determination method for κ_{lat} which is more precise than our approximation from the Wiedemann-Franz law.

A direct property comparison of WO₂, WO_{2.72}, WO_{2.90} and WO₃ can be conducted up to the maximum temperature $T = 863 \text{ K}$ at which WO_{2.72} was investigated. Here WO_{2.90} exhibits the highest Seebeck coefficient with $\alpha = -55 \mu\text{V}\cdot\text{K}^{-1}$ in contrast to WO_{2.72} and WO₂ with $-24 \mu\text{V}\cdot\text{K}^{-1}$ and $-22 \mu\text{V}\cdot\text{K}^{-1}$ respectively (Figure S2a).

The figures of merit ZT at $T = 860 \text{ K}$ are low (0.006, 0.017 and 0.045 for WO₂, WO_{2.72} and WO_{2.90}, respectively, Figure S2b). Maximum $ZT = 0.061$ is found for WO_{2.90} at 963 K. The low Seebeck coefficient is a drawback for WO_{2.72} and WO₂, together with the high κ_{lat} of WO₂. However, in the measured temperature range none of the materials shows a ZT maximum as of yet.

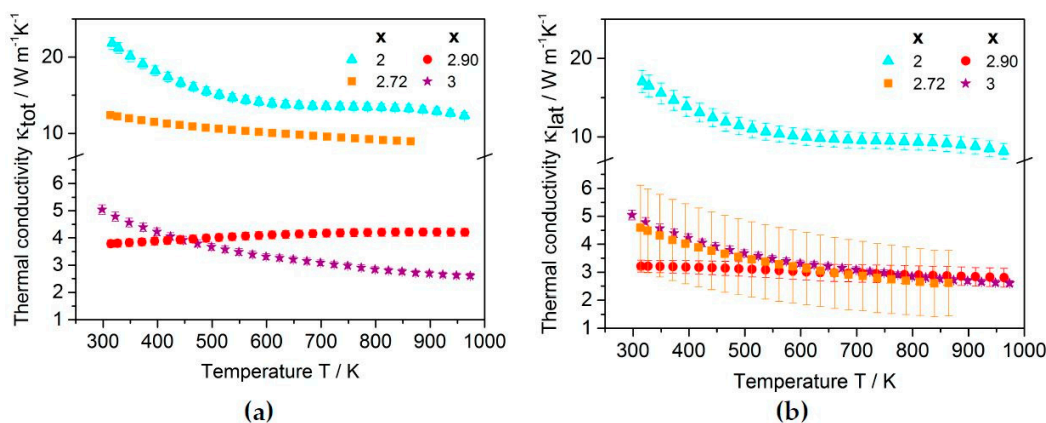


Figure 6. Thermal conductivity of the oxides WO₂, WO_{2.72}, WO_{2.90} and WO₃: (a) Total thermal conductivity κ_{tot} ; (b) Lattice contribution $\kappa_{\text{lat}} = \kappa_{\text{tot}} - \kappa_{\text{el}}$ with κ_{el} from the Wiedemann-Franz law. Mind the different scales of the broken axis.

2.3. Compositions WO_x

The phase formation in WO_x samples with varying x is established from the PXRD patterns after the SPS-1420 K/10 min treatment (Figure 4). Semi-logarithmic plotting emphasizes reflections with low intensity. In Table 2 the observed phases are listed.

Table 2. Phases observed from PXRD in WO_x samples prepared with SPS-1420 K/10 min (●—observed, □—not observed).

| x | Phases | | | | | |
|-----------|-----------------|---------------------------------|------------------------------------|---------------------------------|--|----------------------------------|
| | WO ₂ | W ₁₈ O ₄₉ | “WO _{2.82} ” ^a | W ₂₀ O ₅₈ | W ₂₅ O ₇₃ ^b | γ/δ -WO ₃ |
| 2 | ● | □ | □ | □ | □ | □ |
| 2.50 | ● | ● | □ | □ | □ | □ |
| 2.72–2.80 | □ | ● | ● | □ | □ | □ |
| 2.82–2.88 | □ | ● | ● | ● | □ | □ |
| 2.90 | □ | □ | □ | ● | □ | □ |
| 2.92–3 | □ | □ | □ | ● | ● | ● |

^a Presumed composition of the new phase. Synchrotron data suggests this to be W₁₂O₃₄. ^b Phase hard to detect due to strong reflection overlapping.

For $x = 2.50$ (Figure 4) only WO_2 (green squares) and $\text{W}_{18}\text{O}_{49}$ ($x = 2.72$, brown rhombs) phases are observed as predicted from the phase diagram (Figure 1a).

In the range $2.72 \leq x \leq 2.90$, only $\text{W}_{18}\text{O}_{49}$ ($x = 2.72$) and $\text{W}_{20}\text{O}_{58}$ ($x = 2.90$) are expected according to the phase diagram. For $2.72 \leq x \leq 2.80$, $\text{W}_{18}\text{O}_{49}$ and an additional phase (black arrows) are observed. With increasing O/W-ratio ($2.82 \leq x \leq 2.88$) the expected reflections of $\text{W}_{20}\text{O}_{58}$ ($x = 2.90$, red dots) appear. The unindexed reflections are most intense for $x = 2.82$. From diffraction data of this sample containing only $\text{W}_{18}\text{O}_{49}$ and the additional phase, we find many reflection positions fitting to the pentagonal column phase $\text{W}_{12}\text{O}_{34}$ ($x = 2.83$) [34]. In our case, the parameters of the monoclinic unit cell are slightly changed to $a = 17.229(1)$ Å, $b = 3.782(1)$ Å, $c = 19.496(1)$ Å and $\beta = 105.77(1)$ (Table 1). This is just a rough suggestion; a structure refinement was not successful yet. Distinct reflections of this phase are found also after a comparative synthesis in evacuated silica tubes, which rules out the SPS as cause for its formation (Figure S3). Attempts on synthesis of this phase as single-phase bulk material and further investigations on the structure are pending.

For $2.92 \leq x \leq 2.98$, the PXRD patterns resemble that of pure WO_3 processed in the SPS: reflections of $\gamma\text{-WO}_3$, $\delta\text{-WO}_3$, $\text{W}_{20}\text{O}_{58}$ ($x = 2.90$) and possibly $\text{W}_{25}\text{O}_{73}$ ($x = 2.92$) occur. A bluish-violet color of all samples with $2.92 \leq x \leq 2.98$ supports the existence of the latter since $\text{W}_{20}\text{O}_{58}$ and $\text{W}_{25}\text{O}_{73}$ are colored deeply blue and violet respectively [14,21]. However, samples with the nominal composition ($x = 2.92$) do not yield single-phase materials. Under SPS conditions, $\text{W}_{25}\text{O}_{73}$ might not be stable.

2.3.1. Microstructure

From polarized light microscopy (PLM), the grain size of all synthesized WO_x samples is found to be of the order 10–30 μm (Figure 7). A color variation from yellow to red to blue with increasing O/W-ratio x is caused by the different optical reflectivity of the occurring phases. According to SEM images with backscattered electron (BSE) contrast, the samples are homogeneous. Distinct porosity is found only for $x = 2$ and 2.98. Energy dispersive X-ray spectroscopy (EDX) reveals tungsten and oxygen only, but differences of the oxygen content are below the detection limit.

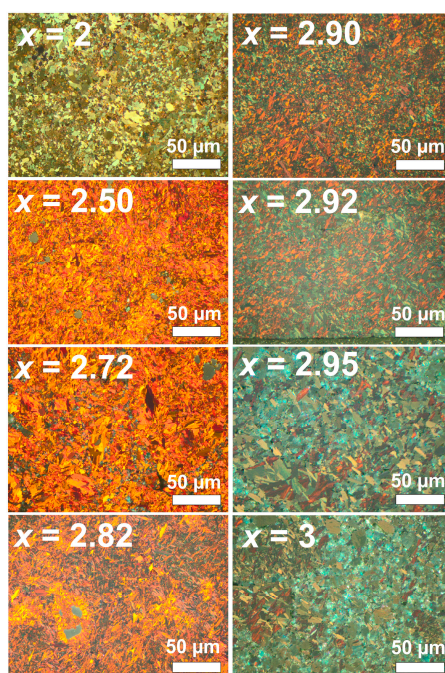


Figure 7. Polarized light microscopy (PLM) of WO_x materials. A yellowish-to-red-to-bluish color variation with increasing O/W-ratio x is observed due to the different optical reflectivity of the occurring phases.

2.3.2. Thermoelectric Properties

The electrical conductivity of the WO_x samples strongly correlates with the O/W-ratio x . When the oxygen concentration is increased to $x \geq 2.90$, there is a continuous decrease of $\sigma(T)$ with minor temperature dependence similar to that of $\text{WO}_{2.90}$ (Figure 8a). According to PXRD (Figure 4), next to $\text{W}_{20}\text{O}_{58}$ the nearly insulating phases δ - and γ - WO_3 occur in this composition range. Thus, the charge carrier concentration and $\sigma(T)$ mainly depend on the $\text{W}_{20}\text{O}_{58}$ content, which decreases with increasing x . The influence of one further phase, possibly $\text{W}_{20}\text{O}_{73}$ ($x = 2.92$), is not known as of yet.

For decreasing O/W-ratio $x < 2.90$, a metallic behaviour is promoted continuously (Figure 8a). The $\sigma(T)$ approaches that of $x = 2.72$ with the increasing $\text{W}_{18}\text{O}_{49}$ ($x = 2.72$) phase content (Figure 4). No discontinuity of $\sigma(T)$ is found for $x = 2.82$ where the highest amount of “ $\text{WO}_{2.82}$ ” is observed. Thus, this phase is electrically conducting. Altogether, the composition $x = 2.90$ is the limit between metallic and nonmetallic behaviour (Figure 8b).

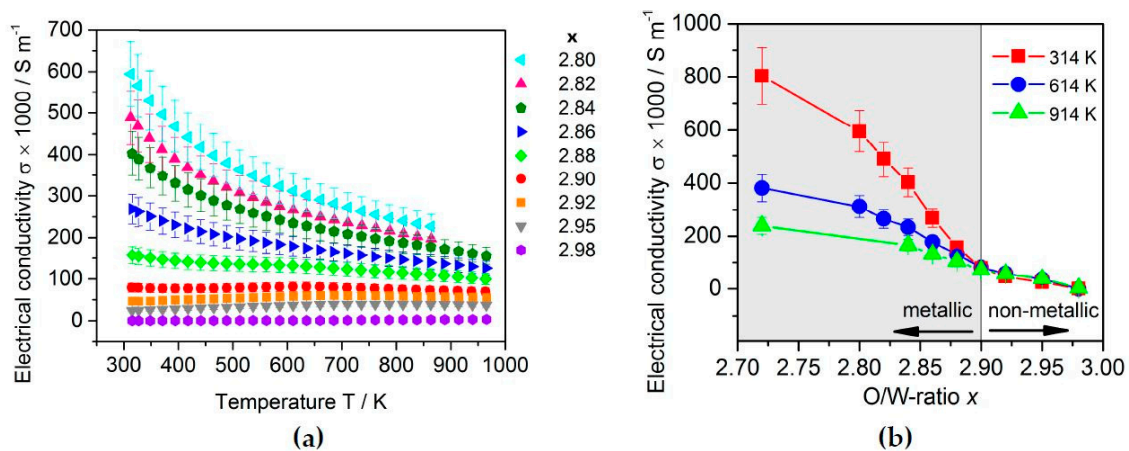


Figure 8. (a) Electrical conductivity $\sigma(T)$ of the WO_x samples ($2.80 \leq x \leq 2.98$); (b) The temperature dependence of $\sigma(T)$ clearly changes from nonmetallic to metallic at $x \approx 2.90$.

A similar trend is observed for the Seebeck coefficient (Figure 9a). Strong non-monotonic behaviour for the composition $x = 2.98$ results from the large amounts of WO_3 in the material (Figure 4) and its therefore near-insulating character during the TE property measurements. The specific influence of the “ $\text{WO}_{2.82}$ ” and $\text{W}_{25}\text{O}_{73}$ ($x = 2.92$) phases cannot be considered yet due the lack of the TE properties of the phase-pure material.

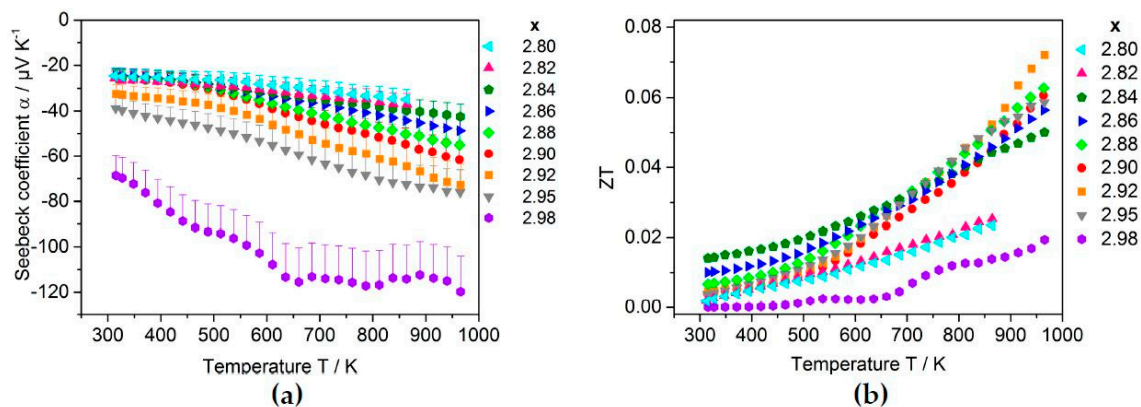


Figure 9. Thermoelectric properties of the WO_x samples ($2.80 \leq x \leq 2.98$): (a) Seebeck coefficient $\alpha(T)$ and (b) resulting figures of merit ZT . Error of $\alpha(T)$ is asymmetric.

The continuous property change of WO_x materials for $2.80 \leq x \leq 3$ also appears in the thermal conductivity κ_{tot} (Figure 10a). With respect to the uncertainty of the Wiedemann–Franz approximation of κ_{el} (Equations (4) and (5)), κ_{lat} is very similar for all samples $x < 2.98$ (Figure 10b). In the composition range $2.90 \leq x \leq 2.95$ where CS plane phases are found (Table 2), the lattice contribution κ_{lat} appears almost temperature-independent. For $T > 550$ K these samples show no significant reduction of κ_{lat} regarding the WO_3 reference sample with respect to the occurring errors. The exceptionally low value for $x = 2.98$ might be the result of porosity also found by microstructure analysis. However, in the three-phase region ($2.82 \leq x \leq 2.88$) of the system (Table 2), a significantly reduced κ_{lat} is found for $x = 2.84$ up to $T \leq 700$ K. This tendency is also noticeable from a plot of κ_{lat} vs. the O/W-ratio x (Figure 10b inset). It indicates that at high temperatures, the lowest κ_{lat} is achieved for WO_x materials with multiple phases due to enhanced phonon scattering at the interfaces.

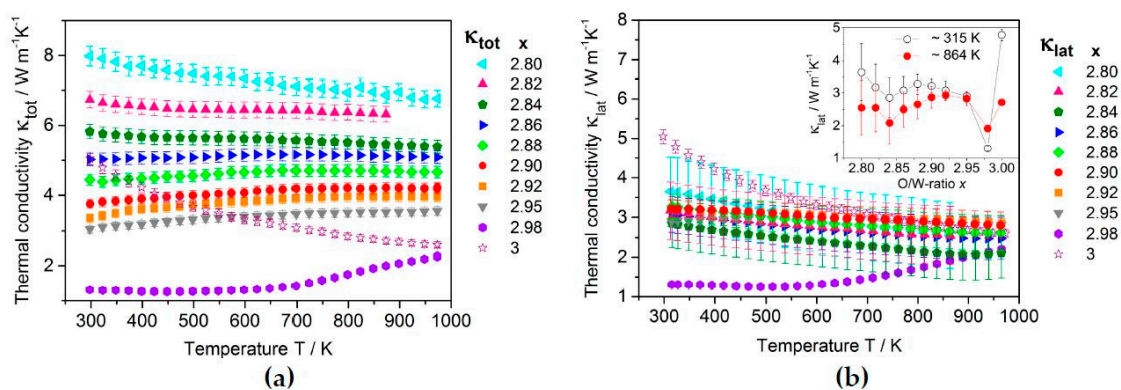


Figure 10. Thermal conductivity of the WO_x samples ($2.80 \leq x \leq 3$): (a) Total thermal conductivity $\kappa_{\text{tot}}(T)$; (b) Lattice contribution $\kappa_{\text{lat}} = \kappa_{\text{tot}} - \kappa_{\text{el}}$ with κ_{el} from the Wiedemann–Franz law. The inset shows the dependency $\kappa_{\text{lat}}(x)$ for 315 K and 864 K.

The resulting ZT for the WO_x compositions are very similar to that of $\text{WO}_{2.90}$ (Figure 9b). For $x = 2.92$, the highest $ZT = 0.072$ is reached at 963 K. An exceptional low ZT is reached for $x = 2.82$ and $x = 2.98$ due to the high κ_{tot} and low $\sigma(T)$ respectively. However, none of the compositions shows a ZT maximum in the measured temperature range as of yet.

3. Materials and Methods

3.1. Materials

The purchased powders of starting materials WO_3 (Alfa Aesar, 99.998 wt %, 10–20 μm), WO_2 (Sigma-Aldrich, 99.99 wt %, <150 μm) and elemental W (Chempur, 99.9 wt %, 8–9 μm) were analyzed regarding crystalline contaminations with PXRD. For the preparation of WO_x samples ($2.50 \leq x \leq 2.98$), WO_3 was manually mixed for 15 min under argon atmosphere with appropriate amounts of W.

3.2. Spark Plasma Sintering

For spark plasma sintering (SPS), graphite dies with diameters of 8 mm or 10 mm (Figure 2b) and a graphite lining were filled with ca. 1 g of starting mixture under argon atmosphere, and processed with a SPS-515 ET Sinter Lab apparatus (Fuji Electronic Industrial Co. Ltd., Tsurugashima, Japan).

3.3. Powder X-ray Diffraction

The starting materials and SPS-processed samples were examined with powder X-ray diffraction (PXRD) on the Guinier camera G670 (HUBER Diffraktionstechnik GmbH & Co., KG, Rimsting, Germany) with $\text{Cu-K}\alpha_1$ radiation ($\lambda = 1.540598$ Å, graphite monochromator, $5^\circ \leq 2\theta \leq 100^\circ$, $\Delta 2\theta = 0.005^\circ$). All PXRD data was compared to the theoretical patterns of known phases (Table 1).

A LaB₆ standard was added to single-phase materials for a subsequent cell parameter determination using the least-square method in the WinCSD software package [38].

3.4. High-Resolution Transmission Electron Microscopy

For high-resolution transmission electron microscopy (HR-TEM), a sample was ground to fine powder and dispersed in methanol. The suspension was loaded on a 100-mesh hexagonal copper grid Quantifoil S7/2 (Quantifoil Micro Tools GmbH, Jena, Germany), which was covered beforehand with a carbon film (2 nm). After a complete drying, HR-TEM imaging was performed on a Tecnai F30 (FEI Technologies Inc., Hillsboro, OR, USA) with a field-emission gun at an acceleration voltage of 300 kV. The point resolution amounted to 1.9 Å, and the information limit amounted to ca. 1.2 Å. The microscope was equipped with a wide-angle slow-scan CCD camera (MultiScan, 2 k × 2 k pixels; Gatan Inc., Pleasanton, CA, USA). TEM images were analyzed with the DigitalMicrograph software (Gatan Inc., Pleasanton, CA, USA).

3.5. Thermoelectric Properties

TE properties were measured for the reference samples $x = \{2, 2.72, 2.90, 3\}$ and the WO_x samples in the range $2.82 \leq x \leq 2.98$. Samples previously powdered for PXRD were compacted with SPS-1320 K/10 min and a heating rate of 75 K·min⁻¹. Subsequently, the mass density ρ was determined with Archimedean method (Table S1).

The thermal diffusivity $D(T)$ was measured by laser flash analysis (LFA) on a LFA 457 MicroFlash (NETZSCH GmbH & Co. Holding KG, Selb, Germany) in vacuum between room temperature and 963 K in steps of 25 K. Subsequent polishing removed a subtle yellow stain from the pellet surface which occurred during the LFA. Differential scanning calorimetry (DSC) measurements of the specific heat capacity $c_p(T)$ yielded values that for all WO_x samples were identical to WO₃ with respect to the measurement error (Figure S4). Thus, for the calculation of the total thermal conductivity

$$\kappa_{\text{tot}}(T) = \rho c_p(T)D(T) \quad (3)$$

(T —absolute temperature) of WO_x and WO₂ there were used theoretic $c_p(T)$ curves for WO₃ and WO₂, respectively [39,40]. After an Archimedean density determination, the microstructure was analyzed with polarized light microscopy (LM), scanning electron microscopy (SEM) and energy dispersive X-ray spectroscopy (EDX). Tetragonal bars with the dimensions $a \approx 1.5$ mm and $b \approx 6$ –8 mm were cut from the pellets using a wire saw (Figure 2c). The measurements of the electrical conductivity $\sigma(T)$ and Seebeck coefficient $\alpha(T)$ were performed perpendicular to the SPS pressure direction along the b -edge on a ZEM-3 (ULVAC-RIKO, Munich, Germany) under low pressure helium from RT to 863 K or 963 K in steps of 25 K. The samples were polished before every measurement. The electronic contribution κ_{el} to the total thermal conductivity and consequently the lattice contribution $\kappa_{\text{lat}} = \kappa_{\text{tot}} - \kappa_{\text{el}}$ were calculated with the Wiedemann–Franz equation

$$\kappa_{\text{el}}(T) = L(T)\sigma(T)T \quad (4)$$

Since for semiconductors the Lorenz number $L(T)$ can strongly deviate from the constant value $L = 2.4453 \times 10^{-8} \text{ W}\Omega\cdot\text{K}^{-2}$ the approximation

$$L(T) = 1.5 + \exp[-|\alpha(T)|/116] \quad (5)$$

was used, which is based on the single parabolic band model with acoustic phonon scattering [41]. Comparative results obtained with constant L show only minor deviations and all trends remain the same. For a comparison with other TE materials, the figure-of-merit ZT was calculated according to

$$ZT = [\alpha^2(T)\sigma(T)T]/\kappa_{\text{tot}}(T). \quad (6)$$

4. Conclusions

According to powder X-ray diffraction (PXRD), a new phase termed as “WO_{2.82}” is observed in the composition range $2.72 \leq x \leq 2.90$ in addition to the expected pentagonal column (PC) phase W₁₈O₄₉ ($x = 2.72$) and crystallographic shear (CS) plane phase W₂₀O₅₈ ($x = 2.90$). The reflection positions of “WO_{2.82}” in the synchrotron pattern of a two-phase W₁₈O₄₉/“WO_{2.82}” sample somewhat fit the PC phase W₁₂O₃₄ ($x = 2.83$) with slightly changed lattice parameters. The synthesis as single-phase material and structure refinement still failed, which indicates that the phase is metastable and its structure needs to be further analyzed.

Single-phase WO_{2.90} material is directly obtained from SPS-1420 K/10 min. Both powder X-ray diffraction (PXRD) and high-resolution transmission electron microscopy (HR-TEM) show disorder of the CS planes. Single-phase WO_{2.70} material is obtained from SPS-1420 K/35 min followed by grinding and SPS-1420 K/5 min.

Electronic transport properties of WO_x materials ($2.80 \leq x \leq 2.98$) from the routine SPS-1420 K/10 min reveal a continuous tunability, practically independent from the phases present in the samples. Both the electrical conductivity $\sigma(T)$ and the thermal conductivity $\kappa_{\text{tot}}(T)$ indicate an increase of the charge carrier concentration with increasing oxygen deficiency. Here, the composition WO_{2.90} is the limit between metallic ($x < 2.90$) and nonmetallic behaviour ($x \geq 2.90$).

The multi-phase character of these samples found by PXRD is crucial for the thermal conductivity. Significant reduction of κ_{lat} regarding WO₃ is found up to 700 K for the three-phase material WO_{2.84}. Thus, for $x < 2.90$ the introduction of multiple phases is a way for reducing the thermal conductivity due to increased phonon scattering at the phase interfaces. The formation of the PC phases in this composition range might have additional influence. In contrast, for $2.90 \leq x \leq 3$, which is the typical range for the formation of CS plane phases, a reduction of κ_{lat} is observed only below 550 K. For high-temperature applications, CS planes might be less appropriate phonon scattering centers.

Supplementary Materials: The following are available online at www.mdpi.com/2073-4352/7/9/271/s1. Figure S1: Electrical conductivity $\sigma(T)$ of the reference materials compositions WO₂, WO_{2.72} and WO_{2.90}; Figure S2: Seebeck coefficient $\alpha(T)$ and resulting figures of merit ZT of the reference materials WO₂, WO_{2.72} and WO_{2.90}; Figure S3: PXRD patterns of WO_{2.90} obtained from heating in an evacuated silica tube at 1370 K for 72 h and from SPS synthesis at similar temperature for 3 h; Figure S4: Specific heat capacity $c_p(T)$ of WO_x materials; Table S1: Mass density ρ_{theo} of tungsten oxide phases calculated from the molar mass M and unit cell volume V . References [42–44] are cited in the supplementary materials.

Acknowledgments: This research was funded by the Deutsche Forschungsgemeinschaft (DFG) through the priority program SPP1959 “Manipulation of Matter Controlled by Electric and Magnetic Fields: Towards Novel Synthesis and Processing Routes of Inorganic Materials”. We acknowledge Yurii Prots for performing the PXRD experiments. Thanks also to Markus Schmidt and Vicky Süß for measurements of the specific heat capacity.

Author Contributions: The project was developed by Igor Veremchuk. Felix Kaiser performed the syntheses, and evaluated the data. Measurements of the transport were performed by Igor Veremchuk. Ulrich Burkhardt analyzed the microstructure. TEM studies were performed by Paul Simon. Important discussions regarding the data interpretation were contributed by Yuri Grin, and Bernd Kieback, who acted as mentor commissioned by the TU Dresden.

Conflicts of Interest: The authors declare no conflicts of interest.

References

1. Terasaki, I.; Sasago, Y.; Uchinokura, K. Large thermoelectric power in NaCo₂O₄ single crystals. *Phys. Rev. B* **1997**, *56*, R12685–R12687. [[CrossRef](#)]
2. Snyder, G.J.; Toberer, E.S. Complex thermoelectric materials. *Nat. Mater.* **2008**, *7*, 105–114. [[CrossRef](#)] [[PubMed](#)]
3. Walia, S.; Balendhran, S.; Nili, H.; Zhuiykov, S.; Rosengarten, G. Transition metal oxides—Thermoelectric properties. *Prog. Mater. Sci.* **2013**, *58*, 1443–1489. [[CrossRef](#)]
4. Kieslich, G.; Cerretti, G.; Veremchuk, I.; Hermann, R.P.; Panthöfer, M.; Grin, Y.; Tremel, W. A chemists view: Metal oxides with adaptive structures for thermoelectric applications. *Phys. Status Solidi A* **2016**, *213*, 1–16. [[CrossRef](#)]

5. Lu, Z.; Zhang, H.; Lei, W.; Sinclair, D.C.; Reaney, I.M. High-Figure-of-Merit Thermoelectric La-Doped A-Site-Deficient SrTiO₃ Ceramics. *Chem. Mater.* **2016**, *28*, 925–935. [[CrossRef](#)]
6. Liang, X. Structure and Thermoelectric Properties of Zinc Based Materials. Doctoral Dissertation, Harvard University, Cambridge, MA, USA, 29 August 2013.
7. Mikami, M.; Ozaki, K. Thermoelectric properties of nitrogen-doped TiO_{2-x} compounds. *J. Phys. Conf. Ser.* **2012**, *379*, 012006. [[CrossRef](#)]
8. Feng, B.; Martin, H.-P.; Börner, F.-D.; Lippmann, W.; Schreier, M.; Vogel, K.; Lenk, A.; Veremchuk, I.; Dannowski, M.; Richter, C.; et al. Manufacture and Testing of Thermoelectric Modules Consisting of B_xC and TiO_x Elements. *Adv. Eng. Mater.* **2014**, *16*, 1252–1263. [[CrossRef](#)]
9. Martin, H.-P.; Pönicke, A.; Kluge, M.; Rost, A.; Conze, S.; Wätzig, K.; Schilm, J.; Michaelis, A. TiO_x-Based Thermoelectric Modules: Manufacturing, Properties, and Operational Behavior. *J. Electron. Mater.* **2016**, *45*, 1570–1575. [[CrossRef](#)]
10. Harada, S.; Tanaka, K.; Inui, H. Thermoelectric properties and crystallographic shear structures in titanium oxides of the Magnéli phases. *J. Appl. Phys.* **2010**, *108*, 083703. [[CrossRef](#)]
11. Kieslich, G.; Veremchuk, I.; Antonyshyn, I.; Zeier, W.G.; Birkel, C.S.; Weldert, K.; Heinrich, C.P.; Visnow, E.; Panthöfer, M.; Burkhardt, U.; et al. Using crystallographic shear to reduce lattice thermal conductivity: High temperature thermoelectric characterization of the spark plasma sintered Magnéli phases WO_{2.90} and WO_{2.722}. *Phys. Chem. Chem. Phys.* **2013**, *15*, 15399. [[CrossRef](#)] [[PubMed](#)]
12. Kieslich, G.; Tremel, W. Magnéli oxides as promising *n*-type thermoelectrics. *AIMS Mater. Sci.* **2014**, *1*, 184–190. [[CrossRef](#)]
13. Migas, D.; Shaposhnikov, V.; Borisenko, V. Tungsten oxides. II. The metallic nature of Magnéli phases. *J. Appl. Phys.* **2010**, *108*, 093714. [[CrossRef](#)]
14. Sundberg, M. The crystal and defect structures of W₂₅O₇₃, a member of the homologous series W_nO_{3n-2}. *Acta Cryst. B* **1976**, *32*, 2144–2149. [[CrossRef](#)]
15. Sundberg, M. Structure and “oxidation behavior” of W₂₄O₇₀, a new member of the {103} CS series of tungsten oxides. *Solid State Chem.* **1980**, *35*, 120–127. [[CrossRef](#)]
16. Sundberg, M.; Zakharov, N.D.; Zibrov, I.P.; Barabanenkov, Y.A.; Filonenko, V.P.; Werner, P. Two high-pressure tungsten oxide structures of W₃O₈ stoichiometry deduced from high-resolution electron microscopy images. *Acta Cryst. B* **1993**, *49*, 951–958. [[CrossRef](#)]
17. Barabanenkov, Y.A.; Zakharov, N.D.; Zibrov, I.P.; Filonenko, V.P.; Werner, P. High-pressure phases in the system W-O-I. Structure of WO_{1.09} by HRTEM. *Acta Cryst. B* **1992**, *48*, 572–577. [[CrossRef](#)]
18. McColm, I.J.; Steadman, R.; Wilson, S.J. Iron-promoted phases in the tungsten-oxygen system. *J. Solid State Chem.* **1978**, *23*, 33–42. [[CrossRef](#)]
19. Stoneham, A.M.; Durham, P.J. The ordering of crystallographic shear planes: Theory of regular arrays. *Phys. Chem. Solids* **1973**, *34*, 2127–2135. [[CrossRef](#)]
20. Wriedt, H.A. O-W (Oxygen-Tungsten). In *Binary Alloy Phase Diagrams*, 2nd ed.; Massalski, T.B., Ed.; ASM International: Materials Park, OH, USA, 1990; Volume 3, pp. 2933–2935.
21. Magneli, A. Structure of β-Tungsten Oxide. *Nature* **1950**, *165*, 356–357. [[CrossRef](#)]
22. Gebert, E.; Ackermann, R.J. Substoichiometry of Tungsten Trioxide; the Crystal Systems of WO_{3.00}, WO_{2.98}, and WO_{2.96}. *Inorg. Chem.* **1966**, *5*, 136–142. [[CrossRef](#)]
23. Berak, J.M.; Sienko, M.J. Effect of oxygen-deficiency on electrical transport properties of tungsten trioxide crystals. *J. Solid State Chem.* **1970**, *2*, 109–133. [[CrossRef](#)]
24. Kieslich, G.; Birkel, C.; Douglas, J.E.; Gaultois, M.; Veremchuk, I.; Seshadri, R.; Stucky, G.D.; Grin, Y.; Tremel, W. SPS-assisted preparation of the Magnéli phase WO_{2.90} for thermoelectric applications. *J. Mater. Chem. A* **2013**, *1*, 13050–13054. [[CrossRef](#)]
25. Kieslich, G.; Burkhardt, U.; Birkel, C.; Veremchuk, I.; Douglas, J.E.; Gaultois, M.; Lieberwirth, I.; Seshadri, R.; Stucky, G.D.; Grin, Y.; et al. Enhanced thermoelectric properties of the *n*-type Magnéli phase WO_{2.90}: Reduced thermal conductivity through microstructure engineering. *J. Mater. Chem. A* **2014**, *2*, 13492–13497. [[CrossRef](#)]
26. Venables, D.; Brown, M. Reduction of tungsten oxides with carbon. Part 1: Thermal analyses. *Thermochim. Acta* **1996**, *282*, 251–264. [[CrossRef](#)]
27. Woodward, P.M.; Sleight, A.W.; Vogt, T. Ferroelectric Tungsten Trioxide. *J. Solid State Chem.* **1997**, *131*, 9–17. [[CrossRef](#)]

28. Gulbransen, E.A.; Andrew, K.F. Kinetics of the Oxidation of Pure Tungsten from 500 to 1300 C. *J. Electrochem. Soc.* **1960**, *107*, 619–628. [[CrossRef](#)]
29. Bamwenda, G.R.; Arakawa, H. The Visible Light Induced Photocatalytic Activity of Tungsten Trioxide Powders. *Appl. Catal. A Gen.* **2001**, *210*, 181–191. [[CrossRef](#)]
30. Bolzan, H.; Kennedy, B.; Howard, C. Neutron Powder Diffraction Study of Molybdenum and Tungsten Dioxides. *Aust. J. Chem.* **1995**, *48*, 1473–1477. [[CrossRef](#)]
31. Magnéli, A. Crystal structure studies on β -tungsten oxide. *Ark. Kemi* **1949**, *1*, 223–230.
32. Viswanathan, K.; Brandt, K.; Salje, E. Crystal structure and charge carrier concentration of $W_{18}O_{49}$. *J. Solid State Chem.* **1981**, *36*, 45–51. [[CrossRef](#)]
33. Lamire, M.; Labbe, P.; Goreaud, M.; Raveau, B. Refining and new analysis of $W_{18}O_{49}$ structure. *Rev. Chim. Miner.* **1987**, *24*, 369–381.
34. Sundberg, M. Structure determination from HREM images: Application to a new binary tungsten oxide. *Chem. Scr.* **1979**, *14*, 161–166.
35. Magnéli, A. Structures of the ReO_3 -type with recurrent dislocations of atoms: ‘homologous series’ of molybdenum and tungsten oxides. *Acta Cryst.* **1953**, *6*, 495–500. [[CrossRef](#)]
36. Vogt, T.; Woodward, P.M.; Hunter, B.A. The High-Temperature Phases of WO_3 . *J. Solid State Chem.* **1999**, *144*, 209–215. [[CrossRef](#)]
37. Molenda, J.; Kubik, A. Transport properties and reactivity of tungsten trioxide. *Solid State Ion.* **1999**, *117*, 57–64. [[CrossRef](#)]
38. Akselrud, L.; Grin, Y. WinCSD: Software package for crystallographic calculations (Version 4). *J. Appl. Cryst.* **2014**, *47*, 803–805. [[CrossRef](#)]
39. NIST Chemical Kinetics Database: Tungsten Oxide (WO_3). Available online: <http://kinetics.nist.gov/janaf/html/O-065.html> (accessed on 20 April 2017).
40. NIST Chemical Kinetics Database: Tungsten Oxide (WO_3). Available online: <http://kinetics.nist.gov/janaf/html/O-047.html> (accessed on 20 April 2017).
41. Hyun-Sik, K.; Gibbs, Z.M.; Tang, Y.; Wang, H.; Snyder, G.J. Characterization of Lorenz number with Seebeck coefficient measurement. *APL Mater.* **2015**, *3*, 041506. [[CrossRef](#)]
42. Wadsley, H.D. Nonstoichiometric Metal Oxides—Order and Disorder. In *Nonstoichiometric Compounds*; Gould, R.D., Ed.; American Chemical Society: Washington, DC, USA, 1963; pp. 23–36. [[CrossRef](#)]
43. Salje, E.K.; Rehmann, S.; Pobell, F.; Morris, D.; Knight, K.S.; Herrmannsdörfer, T.; Dovey, M.T. Crystal structure and paramagnetic behaviour of ϵ - WO_{3-x} . *J. Phys. Condens. Matter* **1997**, *9*, 6563–6577. [[CrossRef](#)]
44. Woodward, P.M.; Sleight, A.W.; Vogt, T. Structure refinement of triclinic tungsten trioxide. *J. Phys. Chem. Solids* **1995**, *56*, 1305–1315. [[CrossRef](#)]



© 2017 by the authors. Licensee MDPI, Basel, Switzerland. This article is an open access article distributed under the terms and conditions of the Creative Commons Attribution (CC BY) license (<http://creativecommons.org/licenses/by/4.0/>).